Sādhanā (2020) 45:13
https://doi.org/10.1007/s12046-019-1243-5

A novel control strategy based on hybrid instantaneous theory decoupled approach for PQ improvement in PV systems with energy storage devices and cascaded multi-level inverter

BUDDHADEVA SAHOO[1], SANGRAM KESHARI ROUTRAY[1,2,*] and PRAVAT KUMAR ROUT[2]

[1]Department of Electrical Engineering, Siksha 'O' Anusandhan University, Bhubaneswar 751030, India
[2]Department of Electrical and Electronics Engineering, Siksha 'O' Anusandhan University, Bhubaneswar 751030, India
e-mail: buddhadeva14@gmail.com; routraysk@gmail.com

MS received 30 November 2018; revised 10 November 2019; accepted 11 November 2019; published online 4 January 2020

Abstract. This paper suggests an innovative control architecture based on hybrid instantaneous theory (HIT) decoupled method for improved power quality (PQ) in a photovoltaic (PV) based microgrid utilizing energy storage devices (ESD). Further, to enhance the PV-ESD performance, an eleven-level cascaded inverter (ECI) with compact size, cost, and increase in voltage level is proposed. By considering the simplicity in design and wider application, an improved perturb and observe (IP&O) method is implemented to operate the PV-ESD system at its optimum power point (OPP). In addition to that, for achieving an improved energy management, a battery-based ESD is integrated into the system. Furthermore, the use of grid LCL filter in PV is investigated with the proposed control law design to reduce the harmonic content. To verify the robustness of the HIT approach based on the harmonics and nonlinearity, various test conditions have been examined under different cases ranging from varying environmental conditions, varying grid demand and ESD charging and discharging situations by using MATLAB/Simulink software.

Keywords. Eleven level cascaded inverter (ECI); power quality (PQ); LCL filter; hybrid instantaneous power theory (HIT); energy storage device (ESD).

1. Introduction

Renewable power sources (RPS) like photovoltaic (PV), wind and fuel cells gain the attraction in comparison to the traditional power sources due to the rise in population, fail to meet the increase in power demand and to prevent climate alteration [1–3]. Looking at the development of PV-ESD based energy generation in the micro-grid environment, there is a necessity to emphasize the research on a novel distributed and protection approaches for low and medium sectors [4–6]. To fulfil the increased power demand with high reliability and security, it is essential to operate the PV-ESD at its optimum PowerPoint (OPP) by using an innovative control method. To regulate the PQ level, a two-stage PV-ESD generating operation generally adopted for better efficiency and performance. At the first stage, a dc–dc converter is used to maintain the constancy of variable dc voltage and in the second stage; a dc–ac inverter is used for grid integration. Yet, this topology leads to a more complex structure and control, and higher cost. To avoid these limitations particularly in real-time applications, this study focuses on the single-stage PV-ESD operation [7–9].

For medium to high power applications like RPS, drives, blower, and fans, etc.; the multi-level inverter (MLI) plays an important role due to its more voltage levels. MLI facilitates reduced error in voltage, non-linearity, and switching losses, and improve electromagnetic interference [10]. Primarily, H-bridge inverters are implemented in the dc–ac conversion schemes [11]. This concept is improved by using a diode clamped inverter (DCI) approach through a set of series capacitors and later on the flying capacitor inverter (FCI) topology based on floating capacitors, replacing the series set of capacitors is largely implemented [12–15]. Later on, frequent other combinational strategies based on a hybrid design concept have developed as an addition to the fundamental strategies [16]. By this idea with fixing a reduced number of electronic switches and increasing in the voltage levels, an improved PQ is achieved in comparison to the primary inverter designs [17, 18]. However, the drawbacks related to the necessity of more switches are the key issues to emphasis on reduction of switches. The implementation of low voltage rating switches to some extent reduces the complication, price and

*For correspondence

size factors, but again each switch requires a gate driver circuit to activate the system. Consequently, deprived of scarifying the performance, design of a reduced switch MLI and gate driver circuit would be an appropriate solution for the above problems.

Microgrid operation and control pretence to resolve certain issues, particularly with significant penetration of RPS like PV based system with the erratic nature of power generation. Besides most distributed power sources (DPSs) in micro-grid as MLI based inverters, firmness and the optimum performance become a major problem due to the decrease in mechanical inertia. In this perception, battery-based ESDs can be pondered as a significant solution due to their capability to reduce the generation and demand fluctuations for flexible power management. Many robust control approaches are suggested for a combined PV-ESD for reducing the PV power variations [19–22]. Though, the combined PV-ESD leads to system intricacy, the possibility of failure, and delays in ESD action. Traditionally, in PV-ESD systems, the battery is integrated to the RPS through two converters, one as the converter to charge/discharge the ESD and another converter for ac conversion. Apart from the necessity of satisfactory control strategy, the economic and size factor needs to be implemented in the above converter strategies. In this paper, the above-related problems are considered to obtain better performance in the case of PV-ESD schemes.

PQ problems associated with real power, reactive power, apparent power, and non-linearity, contained a supervised energy-producing component supposed to be well within the limit under linear load situations. Yet, due to the rising energy demand, unbalanced-load applications, and ambiguity in distributed RPS; the parameters such as balancing the real power, reactive power support, and reduction in non-linearity are the emerging problems considered in numerous studies [22–24]. Lack of appropriate PQ control strategies and filters has triggered the new power schemes to reduce the harmonic contained in the PV-ESD integrated system [25]. Active filter-based mitigation schemes are widely implemented for reducing the voltage and current harmonics in the microgrid applications [25–29]. The main function of shunt power filter (SPF) is to compute the appropriate reference current and to employ in the related control strategies for regulating system parameters during unbalanced and non-linear load conditions. An effort has been taken in this study based on HIT architecture to calculate an appropriate reference current and to attain optimum PQ for a PV-ESD system.

A novel current decomposition technique is projected to compute separately the balanced and distorted current in a three-phase distributed RPS. The control approach is based on the improved version of Akagi's and Peng's power schemes [20, 21], referred as the HIT decoupled approach. The novel current decomposition approach is proposed to design a robust control strategy for MLI control in PV-ESD based grid-following systems. Furthermore, the proposed control approach is capable of decomposing the power signals into a much more detailed component by which it is easier to eliminate the distorted component and make the system more flexible and reliable for practical implementation. The system efficiency is further improved by using a reduced switch ECI by increasing the voltage levels. This paper is more concerned with the design of a grid-following three-phase solar system with the ESD by using a single-stage ECI having the capability of OPP, for grid current and battery current regulation. To validate the practical applicability of the proposed technique, an LCL filter is used to eliminate the non-linearity further to keep within the prescribed limit according to the IEEE-519 and IEEE-1541 standard.

The major focus of the proposed PV-ESD system is presented as follows:

1. Design of an improved control technique based on the HIT decoupled method to calculate an appropriate estimated current by an improved non-linearity cancellation technique.
2. The robust control method is used to separate the balanced and distorted current for eliminating the harmonic component.
3. Application of ECI to PV-ESD microgrid system for better PQ and voltage regulation.
4. Proper battery-based ESD management is suggested for an enhanced power regulation with OPP control.

2. Design of ECI topology

The circuit diagram of the proposed three-phase ECI approach is illustrated in figure 1. The MLI topology is developed by considering 5-capacitors (C_1, C_2, C_3, C_4, and C_5), 10-operational switches ($T_1, T_2, T_3, T_4, T_5, T_6, T_7, T_8, T_9$, and T_{10}) and one traditional voltage source converter (TVSC) [27, 28]. In the developed ECI, the voltage levels and the TVSI switches (S_1, S_2, S_3, S_4, S_5, and S_6) are functioned through the operational switches. As illustrated in figure 1, eleven voltage levels are generated through 5 basic sub-MLI (MLI_{s1}, MLI_{s2}, MLI_{s3}, MLI_{s4}, and MLI_{s5}) are linked through the antiparallel operational switches. To neglect the simultaneous short circuit conditions, the operational switches '$T_1 - T_2$', '$T_3 - T_4$', '$T_5 - T_6$', '$T_7 - T_8$', and '$T_9 - T_{10}$' are not permitted to be concurrently turned ON state. The MLI is functioned for both +ve and −ve half conditions. In the +ve half condition, the MLI is functioned for 6-Cases (*Case* 1 to *Case* 6) of operation and in the −ve half condition, the MLI is functioned for another 6-Cases (*Case* 7 to *Case* 12) of operation, to produce a total of eleven-voltage levels.

Case 1: In this Case, figure 2(a) illustrates that the operational switches 'T_2, T_4, T_6, T_8, and T_{10}', and the TVSC switches 'S_1, S_2, and S_6' are at ON state. For providing a continuous current path, the current transmitted

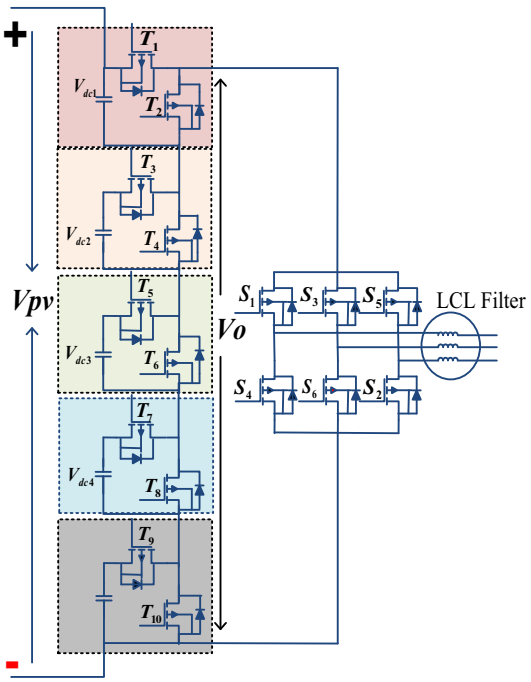

Figure 1. Circuit diagram of ECI.

through the *filter inductor* -T_2-T_4- T_6- T_8-T_{10}-S_1- S_2-S_6- *grid* as indicated in figure 2(a). During this Case, the output voltage of the ECI is computed as zero, because the used capacitors are not in the discharging state.

Case 2: In this Case, figure 2(b) illustrates that the operational switches 'T_1, T_4, T_6, T_8, and T_{10}, and the TVSC switches 'S_1, S_2, and S_6' are at ON state. For providing a continuous current path, the discharged current transmitted through C_1-T_1-S_1-S_2-S_6 -T_8-T_6-T_4- *utility* as indicated in figure 2(b). During this Case, the output voltage of the ECI is computed as V_{dc}, because 'C_1' is at discharging state.

Case 3: In this Case, figure 2(c) illustrates that the operational switches 'T_1, T_3, T_6, T_8, and T_{10}' and the TVSC switches 'S_1, S_2, and S_3' are at ON state. For providing a continuous current path, the discharged current transmitted through C_2-S_3-C_1-S_1-T_1-T_2-T_3-S_{10}-S_8-S_6 *utility* as indicated in figure 2(c). Due to both the capacitors 'C_1 and C_2' are at the discharging state, the output voltage of the ECI is computed as 2 V_{dc}.

Case 4: In this Case, figure 2(d) illustrates that the operational switches 'T_1, T_3, T_5, T_8, and T_{10}' and the TVSC switches 'S_1, S_2, and S_3' are at ON state.

For providing a continuous current path, the discharged current transmitted through C_3-T_5-C_2-T_3-C_1-T_1-S_1-S_2-S_3-T_{10}-T_8- *utility* as indicated in figure 2(d). The output voltage of the ECI is computed as 3 V_{dc}, as all the capacitors 'C_1, C_2, and C_3' are at discharging state.

Case 5: In this Case, figure 2(d) illustrates that the operational switches 'T_1, T_3, T_5, T_7, and T_{10}' and the TVSC switches 'S_2, S_3, and S_4' are at ON state. For providing a continuous current path, the discharged current transmitted through C_4-T_7-C_3-T_5-C_2- T_3-C_1- T_1-S_2-S_3-S_4-T_{10}- *utility* as indicated in figure 2(e). The output voltage of the ECI is computed as 4 V_{dc}, because all the capacitors 'C_1, C_2, C_3, and C_4' are at discharging state.

Case 6: As shown in figure 2(f), the operational switches 'T_1, T_3, T_5, T_7, and T_9', and the TVSC switches 'S_2, S_3, and S_4' are at ON state. For providing a continuous current path, the discharged current transmits through C_5- T_9- C_4- T_7- C_3- T_5- C_2- T_3- C_1- T_1- S_2-S_3-S_4- *utility* as indicated in figure 2(f). As all the capacitors 'C_1, C_2, C_3, C_4 and C_5' are at discharging state, the output voltage of the ECI is computed as 5 V_{dc}.

The proposed ECI produces the voltage levels in the +ve half condition at 0, V_{dc}, 2 V_{dc}, 3 V_{dc}, 4 V_{dc}, and 5 V_{dc} respectively. Likewise, in the −ve half condition, the inverter produces the same voltage levels with the reverse sign. In −ve half condition, the ECI switching arrangements are inverted as compared to the +ve half condition.

As a result, the system is able to generate eleven voltage levels such as 0, $\pm V_{dc}$, $\pm 2V_{dc}$, $\pm 3V_{dc}$, $\pm 4V_{dc}$, and $\pm 5V_{dc}$ respectively. The switching arrangements, as well as the voltage levels of the proposed ECI for both half-cycles, are illustrated in table 1.

3. Control architecture

Figure 3 illustrates the complete test system diagram of PV-ESD based non-linear load system. By using a novel HIT method, the required real and reactive power is supplied to the grid through ECI. To produce optimum power 'P_s', the proposed system is designed through an IP&O tracking technique. By using the OPP algorithm, the required dc-voltage is obtained through the available solar power data. The detailed analysis of the generated reference voltage 'V_s^*' is presented in [7–9].

3.1 *HIT control architecture*

As shown in figure 4, the main objective of the proposed HIT decoupled control approach is to regulate the non-linearity and harmonic contained for boosting the PQ level. The three-phase source/load corresponding voltage and current components are transformed to $\alpha\beta$ components as shown below:

$$V_{g,abc} = \sqrt{\frac{2}{3}} \begin{bmatrix} 1 & 0 & \frac{1}{\sqrt{2}} \\ -\frac{1}{2} & \frac{\sqrt{3}}{2} & \frac{1}{\sqrt{2}} \\ -\frac{1}{2} & -\frac{\sqrt{3}}{2} & \frac{1}{\sqrt{2}} \end{bmatrix} \begin{bmatrix} V_{g,\alpha} \\ V_{g,\beta} \\ V_{g,0} \end{bmatrix} \quad (1)$$

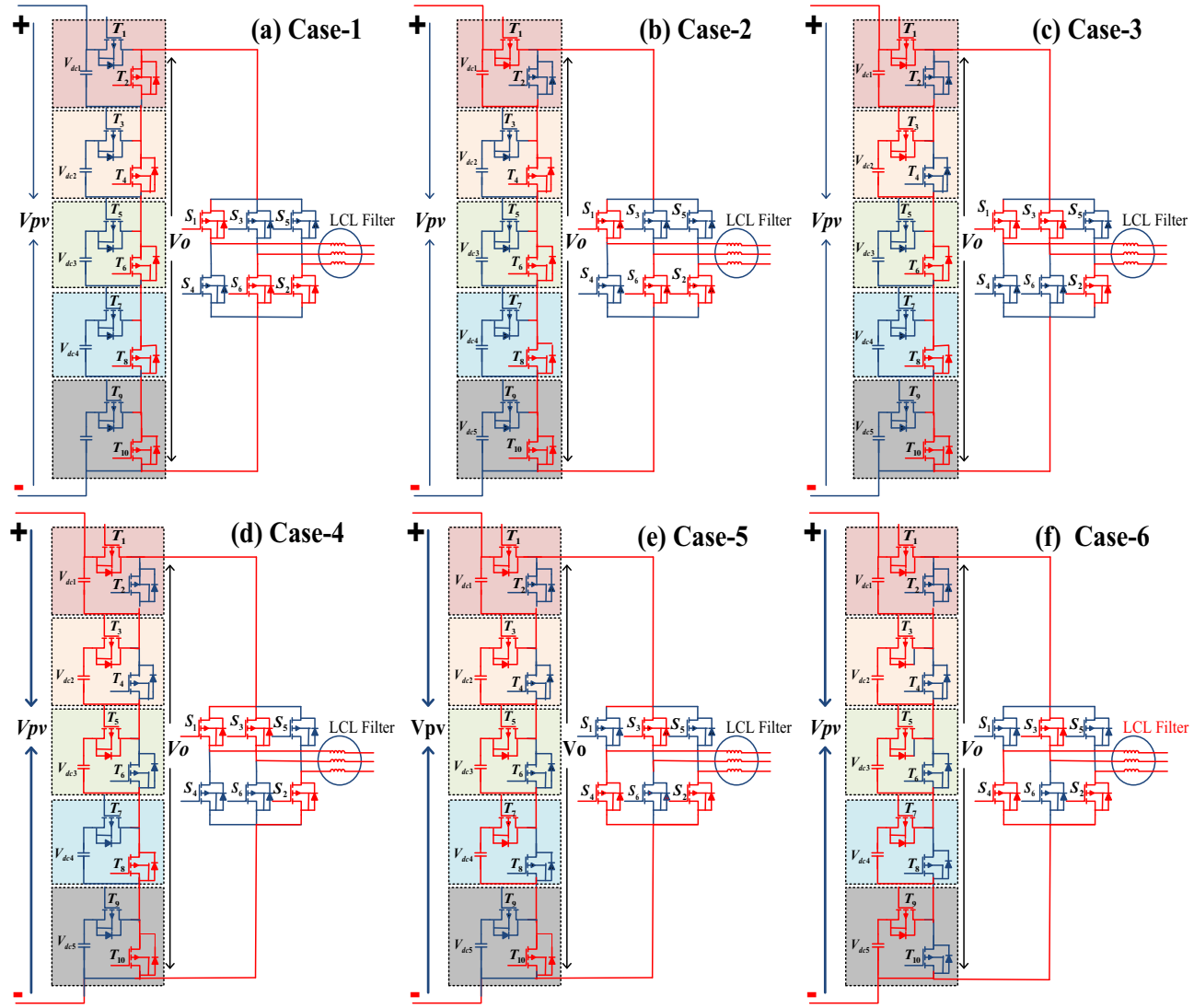

Figure 2. Operational equivalent circuits of RSECI in the positive half cycle. *Red lines indicate the current flow direction.

As per the 3-phase and 3-wire system, the zero-sequence voltage components ($V_{g,0}$) are removed and only ($V_{g,\alpha}$ and $V_{g,\beta}$) components of the voltage are considered for the development of the controller.

$$\begin{bmatrix} V_{g,\alpha} \\ V_{g,\beta} \end{bmatrix} = \sqrt{\frac{2}{3}} \begin{bmatrix} 1 & -\frac{1}{2} & -\frac{1}{2} \\ 0 & \frac{\sqrt{3}}{2} & -\frac{\sqrt{3}}{2} \end{bmatrix} \begin{bmatrix} V_{g,a} \\ V_{g,b} \\ V_{g,c} \end{bmatrix} \tag{2}$$

Likewise, the grid current ($I_{g,\alpha}$ and $I_{g,\beta}$) and load current ($I_{l,\alpha}$ and $I_{l,\beta}$) components of the grid current '$I_{g,abc}$' and load current' $I_{L,abc}$' are computed. The instantaneous power (P_{inst} and Q_{inst}) are computed as

$$\begin{aligned} S_{PQ} &= V \times I^* = (V_\alpha + jV_\beta) + (I_\alpha - jI_\beta) \\ &= (V_\alpha I_\alpha + V_\beta I_\beta) + j(V_\beta I_\alpha - V_\alpha I_\beta) \end{aligned} \tag{3}$$

From Eq. (3), the real 'P_{inst}' and reactive power 'Q_{inst}' of the PV-ESD is computed as

$$\begin{bmatrix} P_{inst} \\ Q_{inst} \end{bmatrix} = \begin{bmatrix} V_\alpha & V_\beta \\ V_\beta & -V_\alpha \end{bmatrix} \begin{bmatrix} I_\alpha \\ I_\beta \end{bmatrix} \tag{4}$$

By solving Eq. (4), I_α and I_β can be determined as

$$\begin{aligned} \begin{bmatrix} I_\alpha \\ I_\beta \end{bmatrix} &= \frac{1}{V_\alpha^2 + V_\beta^2} \begin{bmatrix} V_\alpha & V_\beta \\ V_\beta & -V_\alpha \end{bmatrix} \begin{bmatrix} P_{inst} \\ 0 \end{bmatrix} \\ &+ \frac{1}{V_\alpha^2 + V_\beta^2} \begin{bmatrix} V_\alpha & V_\beta \\ V_\beta & -V_\alpha \end{bmatrix} \begin{bmatrix} 0 \\ Q_{inst} \end{bmatrix} \end{aligned} \tag{5}$$

The real and reactive current components such as '$I_{\alpha,P}$, $I_{\beta,P}$, $I_{\alpha,Q}$and $I_{\beta,Q}$' can be computed as.

Table 1. Switching conditions of the proposed ECI.

	Operating switches										CVSI switches						
Conditions	T_1	T_2	T_3	T_4	T_5	T_6	T_7	T_8	T_9	T_{10}	S_1	S_2	S_3	S_4	S_5	S_6	Output
Case 1	✗	✔	✗	✔	✗	✔	✗	✔	✗	✔	✔	✔	✗	✗	✗	✔	0
Case 2	✔	✗	✗	✔	✗	✔	✗	✔	✗	✔	✔	✔	✗	✗	✗	✔	V_{dc}
Case 3	✔	✗	✔	✗	✗	✔	✗	✔	✗	✔	✔	✔	✔	✗	✗	✗	2 V_{dc}
Case 4	✔	✗	✔	✗	✔	✗	✗	✔	✗	✔	✔	✔	✔	✗	✗	✗	3 V_{dc}
Case 5	✔	✗	✔	✗	✔	✗	✔	✗	✗	✔	✗	✔	✔	✔	✗	✗	4 V_{dc}
Case 6	✔	✗	✔	✗	✔	✗	✔	✗	✔	✗	✗	✔	✔	✔	✗	✗	5 V_{dc}
Case 7	✔	✗	✔	✗	✔	✗	✔	✗	✔	✗	✗	✗	✔	✔	✔	✗	− 5 V_{dc}
Case 8	✗	✔	✔	✗	✔	✗	✔	✗	✔	✗	✗	✗	✔	✔	✔	✗	− 4 V_{dc}
Case 9	✗	✔	✗	✔	✔	✗	✔	✗	✔	✗	✗	✗	✗	✔	✔	✔	− 3 V_{dc}
Case 10	✗	✔	✗	✔	✗	✔	✔	✗	✔	✗	✗	✗	✗	✔	✔	✔	− 2 V_{dc}
Case 11	✗	✔	✗	✔	✗	✔	✗	✔	✔	✗	✔	✔	✗	✗	✗	✔	− V_{dc}
Case 12	✗	✔	✗	✔	✗	✔	✗	✔	✗	✔	✔	✔	✗	✗	✗	✔	0

*✔ and ✗ denote as the switches ON and OFF condition respectively.

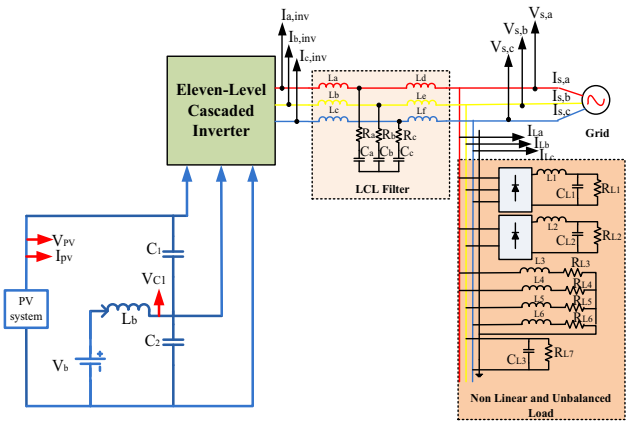

Figure 3. PV-ESD based non-linear system.

$$\begin{bmatrix} I_{\alpha P} \\ I_{\beta P} \end{bmatrix} = \frac{1}{V_\alpha^2 + V_\beta^2} \begin{bmatrix} V_\alpha & V_\beta \\ V_\beta & -V_\alpha \end{bmatrix} \begin{bmatrix} P_{inst} \\ 0 \end{bmatrix} \quad (6)$$

$$\begin{bmatrix} I_{\alpha Q} \\ I_{\beta Q} \end{bmatrix} = \frac{1}{V_\alpha^2 + V_\beta^2} \begin{bmatrix} V_\alpha & V_\beta \\ V_\beta & -V_\alpha \end{bmatrix} \begin{bmatrix} 0 \\ Q_{inst} \end{bmatrix} \quad (7)$$

In figure 4, the obtained optimum solar power 'P_s' is compared with the required grid power of the grid 'P_g', to generate the stable real power 'P_b'. The required grid or stable reactive power '$Q_g = Q_b$' is computed from the grid side measurement.

The real and reactive stable grid current components '$I_{g\alpha,P}$, $I_{g\beta,P}$, $I_{g\alpha,Q}$ and $I_{g\beta,Q}$' can be computed as

$$\begin{bmatrix} I_{g\alpha,P} \\ I_{g\beta,P} \end{bmatrix} = \frac{1}{V_\alpha^2 + V_\beta^2} \begin{bmatrix} V_\alpha & V_\beta \\ V_\beta & -V_\alpha \end{bmatrix} \begin{bmatrix} P_b \\ 0 \end{bmatrix} \quad (8)$$

$$\begin{bmatrix} I_{g\alpha,Q} \\ I_{g\beta,Q} \end{bmatrix} = \frac{1}{V_\alpha^2 + V_\beta^2} \begin{bmatrix} V_\alpha & V_\beta \\ V_\beta & -V_\alpha \end{bmatrix} \begin{bmatrix} 0 \\ Q_b \end{bmatrix} \quad (9)$$

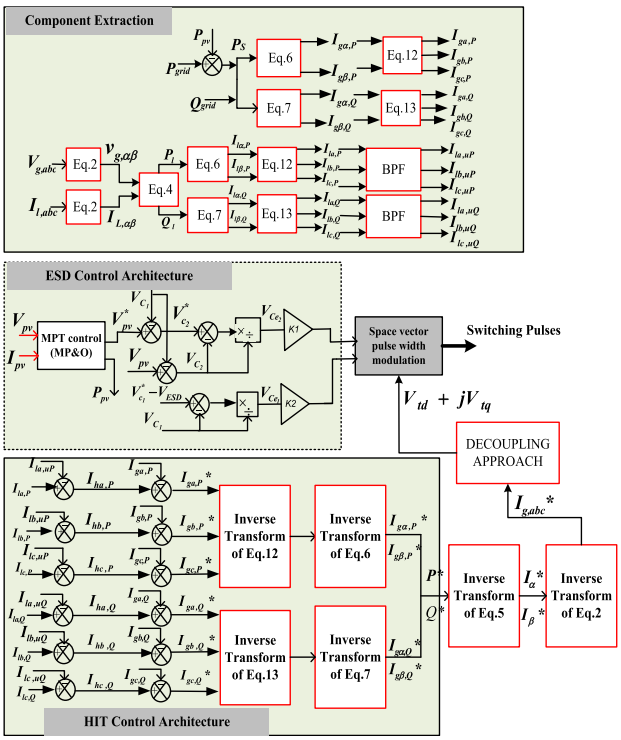

Figure 4. Proposed HIT control architecture diagram.

From Eq. (8) and Eq. (9), the components are transformed to compute stable real and reactive grid current components in abc reference frame such as ($I_{ga,P}$, $I_{gb,P}$, $I_{gc,P}$, $I_{ga,Q}$, $I_{gb,Q}$, $I_{gc,Q}$) through an inverse transformation of Eq. (2). By using the grid voltage '$V_{g,abc}$' and load current '$I_{l,abc}$', the unstable real power 'P_l' and reactive power 'Q_l' are computed.

The real and reactive oscillating load current components '$I_{l\alpha,P}$, $I_{l\beta,P}$, $I_{l\alpha,Q}$and $I_{l\beta,Q}$' are computed as

$$\begin{bmatrix} I_{l\alpha,P} \\ I_{l\beta,P} \end{bmatrix} = \frac{1}{V_\alpha^2 + V_\beta^2} \begin{bmatrix} V_\alpha & V_\beta \\ V_\beta & -V_\alpha \end{bmatrix} \begin{bmatrix} P_l \\ 0 \end{bmatrix} \quad (10)$$

$$\begin{bmatrix} I_{l\alpha,Q} \\ I_{l\beta,Q} \end{bmatrix} = \frac{1}{V_\alpha^2 + V_\beta^2} \begin{bmatrix} V_\alpha & V_\beta \\ V_\beta & -V_\alpha \end{bmatrix} \begin{bmatrix} 0 \\ Q_l \end{bmatrix} \quad (11)$$

From Eq. (10) and Eq. (11), the sinusoidal abc oscillating real and reactive load current components '$I_{la,P}$, $I_{lb,P}$, $I_{lc,P}$, $I_{la,Q}$, $I_{lb,Q}$, and $I_{lc,Q}$' are computed as

$$\begin{bmatrix} I_{la,P} \\ I_{lb,P} \\ I_{lc,P} \end{bmatrix} = \sqrt{\frac{2}{3}} \begin{bmatrix} 1 & 0 \\ -\frac{1}{2} & \frac{\sqrt{3}}{2} \\ -\frac{1}{2} & -\frac{\sqrt{3}}{2} \end{bmatrix} \begin{bmatrix} I_{l\alpha,P} \\ I_{l\beta,P} \end{bmatrix} \quad (12)$$

$$\begin{bmatrix} I_{la,Q} \\ I_{lb,Q} \\ I_{lc,Q} \end{bmatrix} = \sqrt{\frac{2}{3}} \begin{bmatrix} 1 & 0 \\ -\frac{1}{2} & \frac{\sqrt{3}}{2} \\ -\frac{1}{2} & -\frac{\sqrt{3}}{2} \end{bmatrix} \begin{bmatrix} I_{l\alpha,Q} \\ I_{l\beta,Q} \end{bmatrix} \quad (13)$$

The real and reactive oscillating load current components hold both distorted and unstable current components. The above two features are easily parted through a band-pass filter (BPF) at 50 Hz cut-off frequency. As illustrated in figure 4, the oscillating current is transmitted through the BPF, to produce the unstable real and reactive '$I_{la,uP}$, $I_{lb,uP}$, $I_{lc,uP}$, $I_{la,uQ}$, $I_{lb,uQ}$, and $I_{lc,uQ}$' current components respectively. After the unstable load current, the distorted real and reactive current '$I_{ha,P}$, $I_{hb,P}$, $I_{hc,P}$, $I_{ha,Q}$, $I_{hb,Q}$, and $I_{hc,Q}$' components are obtained as

$$I_{ha,P} = I_{la,P} - I_{la,uP} \quad (14)$$

$$I_{hb,P} = I_{lb,P} - I_{lb,uP} \quad (15)$$

$$I_{hc,P} = I_{lc,P} - I_{lc,uP} \quad (16)$$

$$I_{ha,Q} = I_{la,Q} - I_{la,uQ} \quad (17)$$

$$I_{hb,Q} = I_{lb,Q} - I_{lb,uQ} \quad (18)$$

$$I_{hc,Q} = I_{lc,Q} - I_{lc,uQ} \quad (19)$$

The real and reactive distorted current components are attained by comparing the oscillating real and reactive current components with unstable real and reactive current component. To produce the instantaneous real and reactive reference current ($I^*_{ga,P}$, $I^*_{gb,P}$, $I^*_{gc,P}$, '$I^*_{ga,Q}$, $I^*_{gb,Q}$,and $I^*_{gc,Q}$') for ECI conduction, the harmonic active and reactive current components are compared with the produced sinusoidal stable real and reactive current components ('$I_{ga,P}$, $I_{gb,P}$, $I_{gc,P}$', and '$I_{ga,Q}$, $I_{gb,Q}$, $I_{gc,Q}$') as follows.

$$I^*_{ga,P} = I_{ga,P} - I_{ha,P} \quad (20)$$

$$I^*_{gb,P} = I_{gb,P} - I_{gb,P} \quad (21)$$

$$I^*_{gc,P} = I_{gc,P} - I_{hc,P} \quad (22)$$

$$I^*_{ga,Q} = I_{ga,Q} - I_{ha,Q} \quad (23)$$

$$I^*_{gb,Q} = I_{gb,Q} - I_{hb,Q} \quad (24)$$

$$I^*_{gc,Q} = I_{gc,Q} - I_{hc,Q} \quad (25)$$

As shown in figure 4, by using the inverse transform of Eq. (14) and Eq. (15), the sinusoidal reference active and reactive current '$I^*_{ga,P}$, $I^*_{gb,P}$, $I^*_{gc,P}$', '$I^*_{ga,Q}$, $I^*_{gb,Q}$, and $I^*_{gc,Q}$' are transformed to the reference $\alpha\beta$ real and reactive current '$I_{g\alpha,P}$*, $I_{g\beta,P}$*, $I_{g\alpha,Q}$*, and $I_{g\alpha,Q}$*'. After producing the reference real and reactive current, by using Eq. (6) and Eq. (7), the reference real and reactive power (P*and Q*) is computed. As shown in figure 4, the reference current for the ECI operation is obtained through inverse transform of Eq. (9).

The dq control architecture is demonstrated in figure 5. To produce the required reference voltage vector V^* for ECI action, the reference current $I^*_{g,abc}$ is transmitted through decoupling architecture. The grid voltage $V_{g,abc}$, grid current $I_{g,abc}$ and reference current $I^*_{g,abc}$ are converted from abc to dq reference frame as follows.

$$\begin{bmatrix} V_d \\ V_q \end{bmatrix} = \sqrt{\frac{2}{3}} \begin{bmatrix} 1 & -\frac{1}{2} & -\frac{1}{2} \\ 0 & \frac{\sqrt{3}}{2} & -\frac{\sqrt{3}}{2} \end{bmatrix} \begin{bmatrix} V_a \\ V_b \\ V_c \end{bmatrix} \quad (26)$$

$$\begin{bmatrix} I_{S,d} \\ I_{S,q} \end{bmatrix} = \sqrt{\frac{2}{3}} \begin{bmatrix} 1 & -\frac{1}{2} & -\frac{1}{2} \\ 0 & \frac{\sqrt{3}}{2} & -\frac{\sqrt{3}}{2} \end{bmatrix} \begin{bmatrix} I_{S,a} \\ I_{S,b} \\ I_{S,c} \end{bmatrix} \quad (27)$$

$$\begin{bmatrix} I^*_{S,d} \\ I^*_{S,q} \end{bmatrix} = \sqrt{\frac{2}{3}} \begin{bmatrix} 1 & -\frac{1}{2} & -\frac{1}{2} \\ 0 & \frac{\sqrt{3}}{2} & -\frac{\sqrt{3}}{2} \end{bmatrix} \begin{bmatrix} I^*_{S,a} \\ I^*_{S,b} \\ I^*_{S,c} \end{bmatrix} \quad (28)$$

After the transformation, the dq components are passed through PI regulator to produce the control signals (u_{dc} and

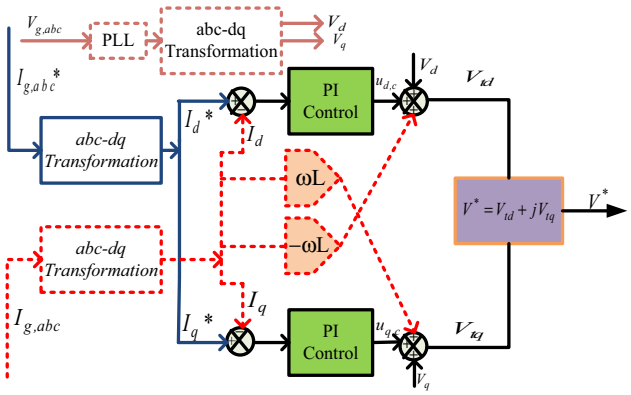

Figure 5. Decoupled control architecture diagram.

u_{qc}). The inverter output voltage is controlled by the control law as [29]:

$$V_{td} = u_{dc} - L_t \omega I_{eq} + V_d \tag{29}$$

$$V_{tq} = u_{qc} + L_t \omega I_{ed} + V_q \tag{30}$$

Where V_{td} and V_{tq} represent as the terminal 'd' and 'q' axis voltage of the inverter. The 'L_t' represents the terminal line parameter of the filter. From $V_{td}$and V_{tq}, the reference voltage vector for ECI is computed. The switching signals for the suggested ECI are generated by using the space vector modulation methods (SVPWM). For SVPWM action, the reference voltage vector is used to choose an appropriate sector in the vector illustration.

3.2 *Control architecture for ESD*

The control method adopted for ESD operation is indicated in figure 4. The capacitor charging and discharging condition also depends upon the proper selection of the short vector applied to the SVPWM method. The proper selection of short vector is attained as per the relative voltage error of the capacitors V_{Ce_1} and V_{Ce_2}.

$$V_{Ce_1} = \frac{V^r_{C_1} - V_{C_1}}{V_{C_1}} \tag{31}$$

$$V_{Ce_2} = \frac{V^r_{C_2} - V_{C_2}}{V_{C_2}} \tag{32}$$

where $V^r_{C_1}$ and $V^r_{C_2}$ are the essential capacitor voltages at C_1 and C_2 respectively. $V_{C_1}$and V_{C_2}symbolize the real capacitor voltages of C_1 and C_2. To select the suitable short vector by using the above components, an appropriate function 'S' is derived as

$$S = T_1 V_{Ce_1} - T_2 V_{Ce_2} \tag{33}$$

where 'T_1 and T_2' are the gains linked with each of $V_{Ce_1}$and V_{Ce_2}respectively. V_{C_1} and V_{C_2} in a traditional neutral point clamped inverter is regulated by equalizing the gains at an equal constant value and also equal to the obtained reference voltage. However, for better regulation of the proposed PV-ESD system during unstable capacitor voltages, the 'T_1 and T_2' are chosen differently.

$$V^r_{C_1} = V_{ESD} \tag{34}$$

$$V^r_{C_2} = V^*_s - V_{C_1} \tag{35}$$

where V_b represents the ESD voltage and V^*_s represents the reference PV voltage obtained from the MPT block. From Eq. (33) , the gain T_2 value is set much higher than T_1 to operate the solar module at its MPP. The charging and discharging condition of the ESD is regulated by using V_{C_1}. During the system operation, the polarity of 'S' decides the charging/discharging condition of ESD. When 'S' is +ve, the C_1 is at charging state and C_2 is at discharging state during that specific period. The inverted operation for C_1 and C_2 occurs during 'S' at negative polarity.

Figure 4 illustrates the suggested control architecture execution on the ac side based on HIT to control the required real and reactive power (P_g, and Q_g) through the ECI operation. In addition, a new SVPWM based short vector selection technique is adopted. On the dc side, the MPT condition is achieved, by implementing a strict control for V_{C_2} (at $T_2 >> T_1$) with the reference value of C_2 $\left(V^r_{C_2} = V^*_s - V_{C_1}\right)$ and also to achieve flexible control for the C_1 voltage (V_{C_1}) with the reference ESD voltage $\left(V^r_{C_1} = V_{ESD}\right)$. '$S$' is used with the computed reference values, to generate an appropriate short vector for the ECI switching operation. On the ac side, by generating the suitable short vector the required real grid power P_g is transmitted to the grid. This, in turn, regulates the capacitor voltage V_{C_1} automatically such that the excess power $(P_s - P_g)$ is charged the ESD or the shortage power $(P_g - P_s)$ is discharged the ESD.

4. Result analysis

The complete test system comprises PV generating unit, ESD unit and ECI with the HIT decoupled control technique which is illustrated in figure 5. To validate the effectiveness of the proposed approach for micro-grid real-time application, it has been simulated through the MATLAB/Simulink environment. An LCL filter is applied to filter out the presence of non-linearity and also used to protect the PV-ESD during any transient condition. The undertaken system parameters of the proposed PV-ESD approach are shown in [29].

Three solar modules are connected in series to fulfil the load and grid demand. The undertaken mathematical equation for the PV unit is taken from Ref. to [4] as

$$I_{pv} = I_{sc} - 10^{-7}\left(e^{\left(\frac{V_{pv}}{2574*10^{-3}}\right)} - 1\right) \tag{36}$$

where I_{pv}, I_{sc}, and V_{pv} represent as the PV current, short-circuit current of the solar unit, and instantaneous PV output voltage respectively. Under standard testing condition (STC) at 1000 W/m^2 irradiance, the short-circuit current I_{sc} and the open-circuit voltage V_{oc} of the PV unit is chosen as 6.04 A and 44 V respectively.

As discussed in the control architecture section, to attain the MPT condition and for the smooth transition of ESD, the value of 'T_2' is chosen greater than 'T_1'. In the design process, it is concluded that any larger value above 100 is suitable for K_2, to select the appropriate short vector. For offering an improved dc voltage (V_{pv}) regulation, the gain value T_2 is chosen as 200.

By seeing the uncertainty, the design of battery inductor L_b plays a key role in smoothening the battery current regulation. A slight change in the inductor also rises the overshoot current of the ESD. In addition to that, the size of L_b depends upon the corresponding capacitor ratings and uncertainty in the voltage conditions. However, by considering the size and cost aspects of the system, 5 mH ratings of L_b is chosen in this study. For showing the variability of the HIT controller, a combined unbalanced and non-linear load is linked to the stable three-phase grid as illustrated in figure 4. The PV-ESD system is tested by changing the reference inputs under subsequent situations.

1. At persistent solar irradiance, PV-ESD system is verified for a step-change in the required real and reactive power.
2. By changing the solar irradiance in a stepwise method, the PV-ESD approach is verified for a constant real and reactive power.
3. At persistent solar irradiance, the PV-ESD system is verified by altering a slope controlled required real power.

Furthermore, to show the importance of the proposed HIT architecture, the undertaken PV-ESD outcomes are compared to the traditional control and inverter approach under the above conditions.

4.1 *Traditional PI control-based NPC inverter without non-linear load applications*

4.1*a First test Case:* In this test Case, the results of the traditional approach are investigated by using the fixed irradiance. In the traditional approach, a neutral point clamped inverter (NPC) is used with the PI control to generate the desired active and reactive power. To achieve the desired power, the inverter generates the desired voltage level by using more power electronic switches, diodes and capacitors. NPC inverter is used to generate three-level output voltage components by using 12 power electronic switches, six diodes, and two capacitors. As a result, the system is well capable of generating the desired voltage and current. The corresponding output voltage waveform of the NPC inverter is shown in figure 6.

Figure 7(a) clearly shows that the NPC inverter contains more harmonics in the output current I_{inv} due to the use of more power electronic switches with the traditional PI controller. The test system is investigated without any non-linear load. As shown in figure 7(b), the harmonic content of the inverter output current I_{inv} is calculated as 5.38% by using Fast Fourier Transform (FFT) analysis. As per the IEEE-1541 standard, the THD value is very high. For the real-time application, it is essential to see the effect of using the non-linear load condition which generally deteriorates the power quality condition. With the objective to restrict the harmonic under nonlinear load condition within the standard value, the proposed approach is suggested as an improvement of inverter capability with adequate control strategy integration specifically in a PV-ESD based microgrid system.

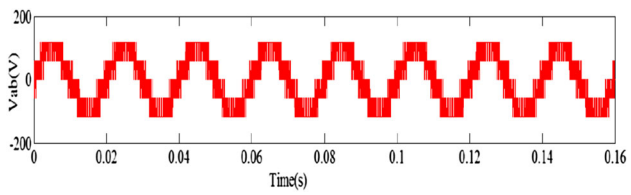

Figure 6. Simulated results: NPCI voltage levels.

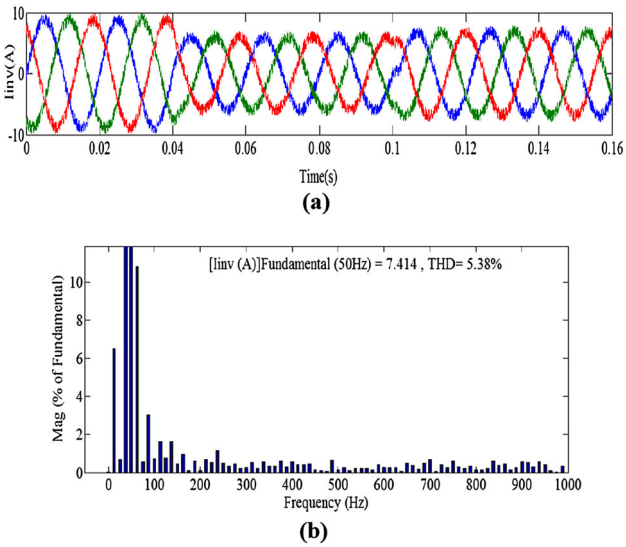

Figure 7. Simulated results: (**a**) NPCI current, (**b**) THD of NPCI current.

4.1b *Second test Case:* In this test Case, the traditional approach is tested by changing the irradiance condition. By using the traditional NPC inverter approach with the PI controller under changing irradiance conditions, the test system generates the desired output voltage and current. As indicated in figure 8(a), due to the high-power electronic switches and fewer voltage levels in the inverter, the output current I_{inv} contains harmonics. Figure 8(b) shows the harmonic content of the inverter current. The harmonic analysis of the output current is analysed by using the FFT technique and the corresponding THD value is 5.68%. The calculated THD is much higher according to the IEEE-1541 standard. Due to the poor control strategy, the traditional multilevel inverter generates more harmonic currents. The above findings motivate to use an RSECI approach with an advanced control strategy to generate a reduced harmonic output current.

4.2 *Proposed HIT control based ECI approach for non-linear load applications*

4.2a *First test Case:* In this test Case, the proposed HIT decoupled control with the ECI approach is tested at the

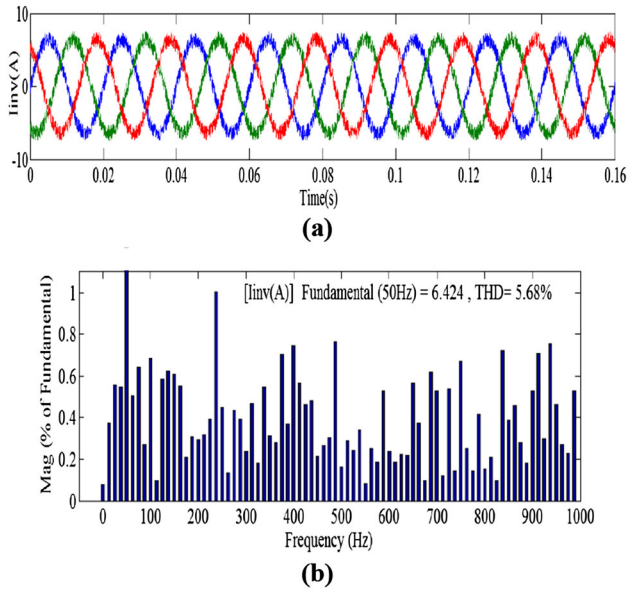

Figure 8. Simulated results: (**a**) inverter current, (**b**) THD of inverter side current.

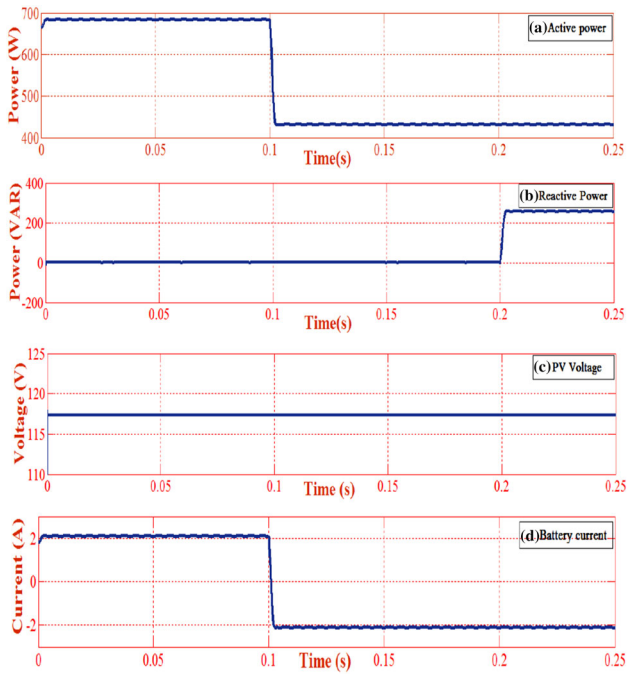

Figure 9. Simulated results: (**a**) active power, (**b**) reactive power, (**c**) PV voltage, (**d**) battery current.

constant environmental condition and the corresponding results are presented in figures 9, 10, and 11 respectively. For this Case study, 'I_{sc}' is chosen as 5.8 A with a fixed solar irradiance condition as calculated through Eq. 33. The required real power demand of the grid is initially set at 682 W and changed to 430 W at a time interval of 100 ms. Similarly, the required reactive power support to the grid is varied from zero to 255 VAR at a time interval of 200 ms.

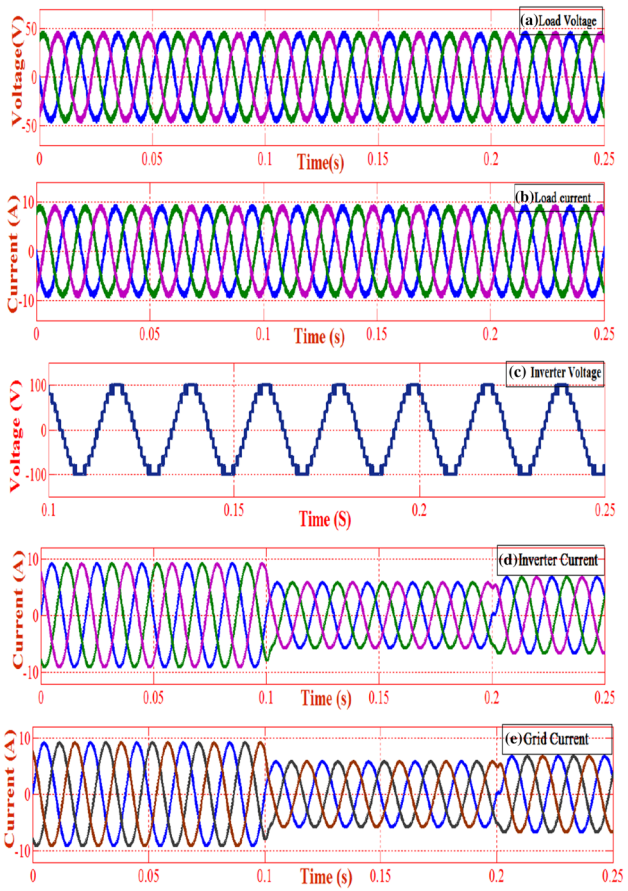

Figure 10. Simulated results: (**a**) load voltage, (**b**) load current, (**c**) inverter output voltage, (**d**) inverter output current, (**e**) grid current.

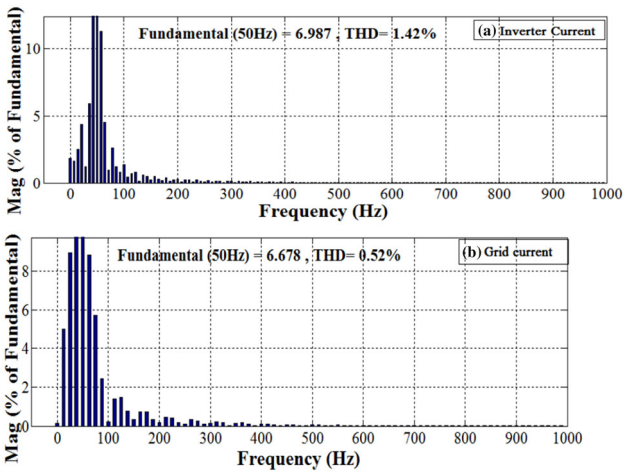

Figure 11. FFT analysis results: (**a**) inverter current, (**b**) grid current.

As per the set condition, the IP&O technique is able to track the required solar module dc voltage 'V_{pv}^{*}' as 117.3 V to achieve the maximum power as 566 W. Figure 9(a, b) indicates that the proposed approach is able to generate the

desired real and reactive power. The desired dc voltage of the test PV-ESD based system is controlled correctly to generate accurate desired power as shown in figure 9(c). When the PV power is more with respect to our utility power requirements, the surplus power is used to charge the storage device and when the PV power is less with respect to the desired power, the battery is used to start discharging. According to the purposed hybrid control approach as indicated in figure 9(d) at 0 ms to 1 ms time interval, the battery discharge at 2.1 A due to the PV generated power insufficient to fulfil the desired amount of grid power, and after 1 ms to 250 ms the battery is used to charge at −2.1 A due to the surplus power of the PV output.

Figure 10(a, b) clearly shows that due to the impact of the nonlinear load, the load voltage and current signal are non-linear and contains more harmonics. Figure 10(c) indicates that the proposed ECI is also able to generate eleven voltage levels by using a smaller number of power electronic switches. As the inverter generates more voltage levels, it is easier to eliminate the harmonics of the grid current and inverter current by using both HIT control architecture and inverter strategy. Figure 11(d, e) shows the results of the inverter side and grid side currents with lesser THD as compared to section 4.1 first Case results. Due to the higher power generation, the inverter current during the time duration 0 ms to 100 ms is 8.8 A. Similarly, for the reduced power generation, the inverter current decreases to 5.72 A during the time interval of 1 ms to 200 ms. At the time 200 ms onwards due to the reactive power injection, the inverter current is further increased to 6.8 A. It indicates that as per our requirements, the inverter current and the grid current are changed.

Compared to the traditional approach as presented in section 4.1 first Case, the inverter based on the proposed approach functions well and generates the current with fewer harmonics. The harmonic distortion factor is calculated by FFT analysis and the corresponding results of inverter current and grid are shown in figure 11(a, b) respectively. As per the FFT analysis, the THD of the inverter and grid current is 1.42% and 0.52%, respectively. In the proposed approach the inverter generates lesser harmonic current comparatively. An LCL filter is used for further reduction of harmonics, as well as to protect the system for the sudden change in voltage and current.

4.2*b Second test Case:* In this test Case, the test results of the proposed HIT decoupled control and RSECI approach are discussed for changing the irradiance condition. The corresponding test results of the proposed approach are shown in figures 12 and 13, respectively. It is assumed that the short circuit current 'I_{sc}' is equal to 4.8 A, 4 A, and 5.4 A at a time interval of 0 ms, 40 ms, and 100 ms, respectively under the changing irradiance condition. The short circuit current of the PV unit is changed at a fixed desired real and reactive power of the system. The desired real power to be transmitted to the utility is set at 482 W and the reactive power as zero.

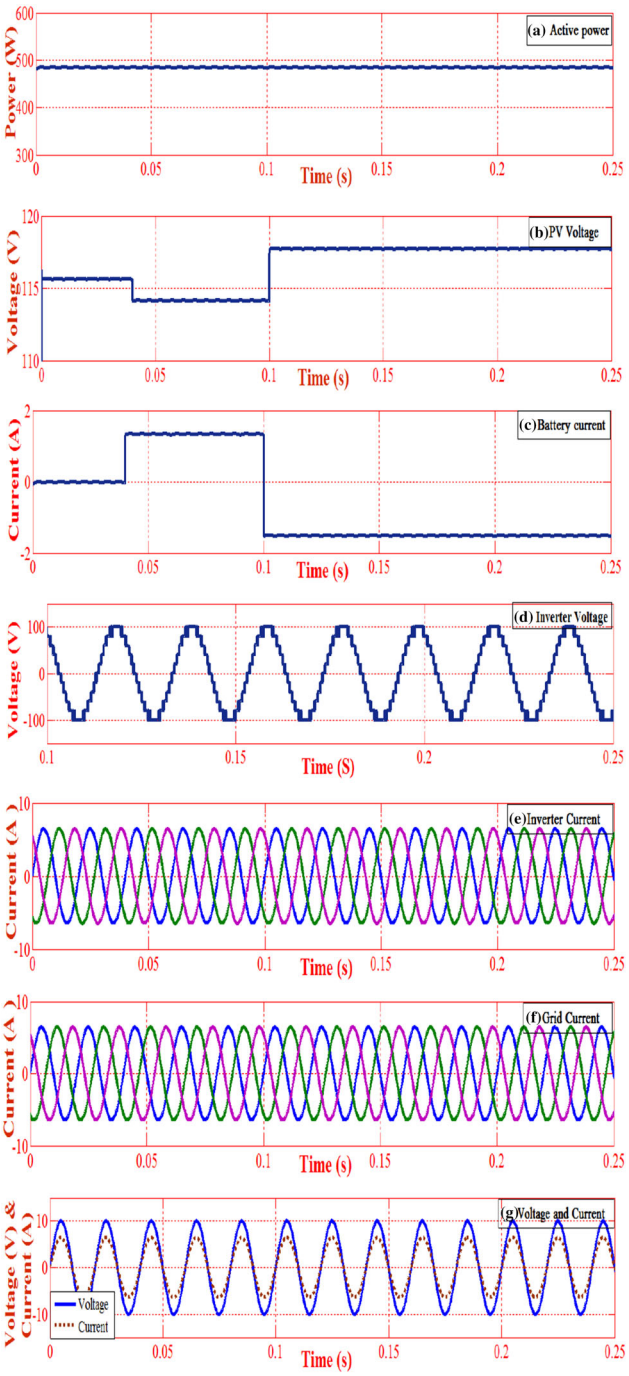

Figure 12. Changing environmental condition simulated results: (**a**) active power, (**b**) PV voltage, (**c**) battery current, (**d**) inverter output voltage, (**e**) inverter output current, (**f**) grid current and (**g**) voltage and current.

As per the above requirement, the IP&O algorithm is able to generate the desired solar module dc voltage 'V_{pv}^{*}' as 115.6 V, 114.1 V, and 117.3 V to attain the maximum power 485 W, 404 W, and 558 W from the test system respectively. Figure 12(a) shows the proposed RSECI able to produce the desired real power. Figure 12(b) shows that by changing the irradiance condition, the PV module

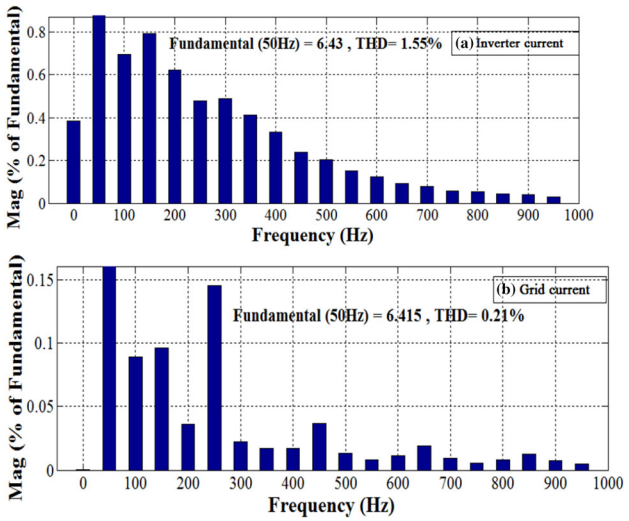

Figure 13. FFT analysis results: (**a**) inverter current, (**b**) grid current.

produces the accurate dc voltage for the generation of maximum power. Figure 12(c) illustrates that the battery adopts a correctly charged and discharged mode of operation to meet the need. Figure 13(c) shows that at 0 ms to 40 ms, the PV power is equal to the desired power, by which the battery cannot be in charge or discharge mode of operation during that period. After that period from 40 ms to 100 ms, the battery is discharged at 1.3 A current to fulfil the grid demand and after 100 ms onwards due to the surplus power of the grid; the battery is charged at − 1.3 A current.

Figure 12(d) indicates that the proposed RSECI is able to generate eleven voltage levels at changing irradiance conditions. As the inverter generates more appropriate voltage levels, it is easier to eliminate the harmonics of the grid current and inverter current by using both HIT control and inverter strategy. Figure 13(e, f) shows the results of the inverter side and grid side currents with lesser THD as compared to the section 4.1 second Case results. The reactive power is zero at all the time. The linear relationship between the single-phase voltage and current is shown in figure 12(g). Compared to the traditional approach as presented in section 4.1 second Case, the proposed approach based inverter is able to offer a fast-transient response and generates the current with fewer harmonics. The harmonic distortion factor is calculated by FFT analysis and the corresponding results of inverter current and grid are shown in figure 13(a, b). As per the FFT analysis, the THD of the inverter and grid current is 1.55% and 0.21%, respectively. In the proposed approach the inverter generates a lesser harmonic current. However, the LCL filter is used to further reduction of harmonics, as well as protect the system for the sudden change in voltage and current.

4.2c *Third test Case:* In this Case, the results of the proposed HIT decoupled control and ECI approach are

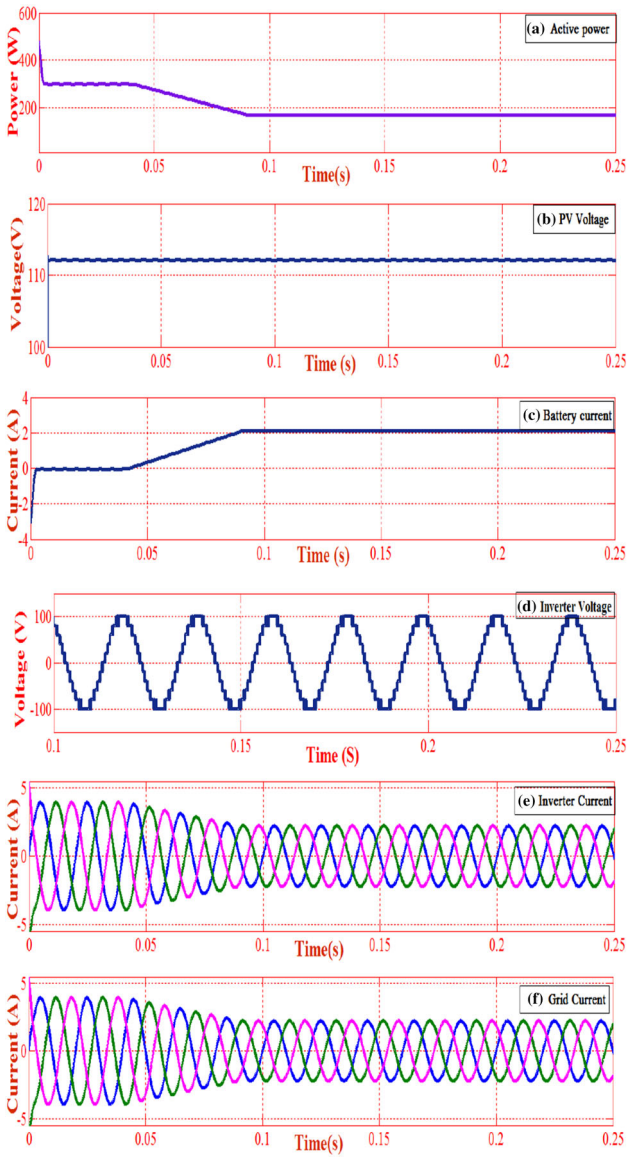

Figure 14. Third test Case results: (**a**) active power, (**b**) PV voltage, (**c**) battery current, (**d**) inverter output voltage, (**e**) inverter output current, (**f**) grid current.

discussed by changing the real power. In this simulation, the desired real power is initially set at 295 W for 40 ms. After 40 ms, the desired real power starts to decrease as a slope-controlled change and finally constant at 165 W for a time 90 ms onwards. According to Eq. (33), it is assumed that the solar irradiation will generate the short circuit current 'I_{sc}' equal to 2.89 A in the PV module. As per the above requirement, the MP&O algorithm is able to generate the desired solar module dc voltage 'V_{pv}^{*}' as 112.8 V to attain the maximum power from the test system, which can produce 305 W of electrical power.

Figure 14(a) shows that as per the grid requirement the real power transferred to the grid decreases gradually and achieves the desired real power at a certain time period.

The generated PV output voltage of the solar system is shown in figure 14(b). Figure 14(c) indicates that the battery charging and discharging conditions of the test system. Initially, at a time interval of 0 ms to 40 ms, the battery current is 0.1 A. Due to the constant PV output power, the reduced amount of power is transferred to the grid, by which the battery charging current is gradually increased and finally set at 2.1 A. In this condition also the inverter is able to generate the desired voltage levels as shown in figure 14(d). Figure 14(e, f) shows the output current of the inverter and grid. As shown in figure 14(e) the inverter current is gradually reduced from 3.4 A at 40 ms and finally stable at 1.9 A at 90 ms. The grid current also follows the same path as per the inverter current.

5. Conclusion

This paper proposed a novel HIT control architecture based decoupled strategy for a PV-ESD system. Further, to enhance the system performance by increasing the power quality, an ECI based MLI is proposed. In this approach, a detailed mathematical control solution for the proposed ECI and ESD is presented in this paper. The results are clearly indicating that by using IP&O technique, the system is able to track maximum power. The PV-ESD system offers better power management, by availing appropriate charging and discharging condition through an improved control strategy. During any uncertainty and transient periods, to protect the system and maintain the improved power quality an LCL filter is integrated. It is able to mitigate the higher-order harmonics of the system. To show the necessity of the proposed controller, the generated proposed PV-ESD obtained results are compared with the traditional PV-ESD results at different operating conditions. The comparative results arrive with justification to the proposed approach as a novel method capable of bringing a better performance with better power quality and flexibility of operation.

References

[1] Paliwal P, Patidar N P and Nema R K 2014 Planning of grid integrated distributed generators: a review of technology, objectives and techniques. *Renew. Sustain. Energy Rev.* 40: 557–570

[2] Eberhard A and Kåberger T 2016 Renewable energy auctions in South Africa outshine feed-in tariffs. *Energy Sci. Eng.* 4(3): 190–193

[3] Castaneda M, Cano A, Jurado F, Sánchez H and Fernandez L M 2013 Sizing optimization, dynamic modeling and energy management strategies of a stand-alone PV/hydrogen/battery-based hybrid system. *Int. J. Hydrogen Energy* 38(10): 3830–3845

[4] Bal S, Anurag A, Nanda M and Sourav S 2015 Comprehensive analysis and experimental validation of an improved mathematical modeling of photovoltaic array. *Advances in power Electronics* 2015: 654092

[5] Orioli A and Di Gangi A 2013 A procedure to calculate the five-parameter model of crystalline silicon photovoltaic modules on the basis of the tabular performance data. *Appl. Energy* 102: 1160–1177

[6] Vijay Muni T, S Srikanth K, Venkatesh N and L Sumedha K 2018 A high performance hybrid MPPT control scheme for a grid connected PV system based three level NPCMLI. *Int. J. Eng. Technol.* 7(2.20): 37–40

[7] Sahoo B, Routray S K and Rout P K 2019 Repetitive control and cascaded multilevel inverter with integrated hybrid active filter capability for wind energy conversion system. *Eng. Sci. Technol. Int. J* 22(3):811–826

[8] Killi M and Samanta S 2015 Modified perturb and observe MPPT algorithm for drift avoidance in photovoltaic systems. *IEEE Trans. Ind. Electron.* 62(9): 5549–5559

[9] Gali V and Hemakumar K 2013 SEPIC converter based photovoltaic system with particle swarm optimization MPPT. *Int. J.* 1(1).

[10] Sahoo B, Routray S K and Rout P K 2019 Artificial neural network-based PI-controlled reduced switch cascaded multilevel inverter operation in wind energy conversion system with solid-state transformer. *Iran. J. Sci. Technol. Trans. Electr. Eng.* 1–21

[11] Bijlenga B, Asplund G, Lundberg P, Jonsson T, Johansson N and Norrga S, ABB A B 2005 *Bidirectional VSC converter with a resonant circuit*. U.S. Patent 6,898,095

[12] Butzmann S and Fink H 2013 Robert Bosch GmbH, Robert Bosch Battery Systems GmbH, Samsung SDI Co Ltd and SB LiMotive Co Ltd, *Battery with Variable Output Voltage*. U.S. Patent Application 13/641,121

[13] Husev O, Roncero-Clemente C, Romero-Cadaval E, Vinnikov D and Jalakas T 2016 Three-level three-phase quasi-Z-source neutral-point-clamped inverter with novel modulation technique for photovoltaic application. *Electr. Power Syst. Res.* 130:10–21

[14] Patnaik S and Panda A K 2013 Real-time performance analysis and comparison of various control schemes for particle swarm optimization-based shunt active power filters. *Int. J. Electr. Power Energy Syst.* 52:185–197

[15] Davies M and Gambach H Siemens A G 2013 *Method for eliminating a fault on a high-voltage dc line*, *system for transmitting an electric current via a high-voltage dc line*, *and converter*. U.S. Patent Application 13/983,240

[16] Colak I, Kabalci E and Bayindir R 2011 Review of multilevel voltage source inverter topologies and control schemes. *Energy Convers. Manag.* 52(2):1114–1128

[17] Samanbakhsh R and Taheri A 2016 Reduction of power electronic components in multilevel converters using new switched capacitor-diode structure. *IEEE Trans. Ind. Electron.* 63(11): 7204–7214

[18] Samsami H, Taheri A and Samanbakhsh R 2017 New bidirectional multilevel inverter topology with staircase cascading for symmetric and asymmetric structures. *IET Power Electron.* 10(11): 1315–1323

[19] Kumar N V, Chinnaiyan V K, Murukesapillay P and Karthikeyan S P 2017 Multilevel inverter topology using single source and double source module with reduced power electronic components. *J. Eng.* (5): 139–148

[20] Kumar D and Zare F 2015 Harmonic analysis of grid connected power electronic systems in low voltage distribution networks. *IEEE J. Emerg. Sel. Top. Power Electron.* 4(1): 70–79

[21] Akagi H, Kanazawa Y and Nabae A 1984 Instantaneous reactive power compensators comprising switching devices without energy storage components. *IEEE Trans. Ind. Appl.* (3): 625–630

[22] Akagi H, Watanabe E H and Aredes M 2017 *Instantaneous power theory and applications to power conditioning*. Wiley, New York

[23] Montanari A A and Gole A M 2016 Enhanced instantaneous power theory for control of grid connected voltage sourced converters under unbalanced conditions. *IEEE Trans. Power Electron.* 32(8): 6652–6660

[24] Czarnecki L S and Haley P M 2015 Power properties of four-wire systems at nonsinusoidal supply voltage. *IEEE Trans. Power Deliv.* 31(2): 513–521

[25] Tummuru N R Mishra M K and Srinivas S 2013 Multifunctional VSC controlled microgrid using instantaneous symmetrical components theory. *IEEE Trans. Sustain. Energy* 5(1): 313–322

[26] Kabiri R, Holmes D G and McGrath B P 2015 Control of active and reactive power ripple to mitigate unbalanced grid voltages. *IEEE Trans. Ind. Appl.* 52(2): 1660–1668

[27] Wang Z, Wu B, Xu D, Cheng M and Xu L 2016 DC-link current ripple mitigation for current-source grid-connected converters under unbalanced grid conditions. *IEEE Trans. Ind. Electron.* 63(8): 4967–4977

[28] Wei Q, Xing L, Xu D, Wu B and Zargari N R 2018 Modulation schemes for medium-voltage PWM current source converter-based drives: an overview. *IEEE J. Emerg. Sel. Top. Power Electron.* 7(2): 1152–1161

[29] Sahoo B, Routray S K and Rout P K 2018 A new topology with the repetitive controller of a reduced switch seven-level cascaded inverter for a solar PV-battery based microgrid. *Eng. Sci. Technol. Int. J.* 21(4): 639–653